

Operation IceBridge sea ice freeboard, snow depth, and thickness data products manual, version 2 processing

Nathan Kurtz and Jeremy Harbeck

1 Overview

The purpose of this document is to describe the retrieval of geophysical data products from the level 1 Operation IceBridge instrument data which can then be used by those wishing to engage in more specialized research. The document describes the retrieval of three important fundamental sea ice properties from the IceBridge data set: 1) sea ice freeboard, 2) snow depth, and 3) sea ice thickness. The known limitations and uncertainties of the derived IceBridge geophysical data products are discussed along with the various input and output parameters. The primary IceBridge data sets which were used in the retrievals are the University of Kansas' snow radar (*Leuschen, 2009*), the Digital Mapping System (DMS) aerial photography (*Dominguez, 2009*), the Continuous Airborne Mapping By Optical Translator (CAMBOT) (*Krabill, 2009*), and the Airborne Topographic Mapper (ATM) laser altimeter (*Krabill, 2009*). The data sets and steps of the production procedure are illustrated in Figure 1.

The IceBridge data set has and will continue evolving in time as instrument changes are made to improve the quality of retrievals from the instrument data. A detailed documentation of the baseline processing steps and justifications for parameter retrieval is provided in *Kurtz et al., [2013]*, while this document outlines the updated version 2 processing effort which corrects errors in the previous data set and also utilizes improved techniques for more accurate determination of sea ice thickness. Sections 2-6 provide an up-to-date description of the primary processing method, while Section 7 lists changes and their associated justifications which were

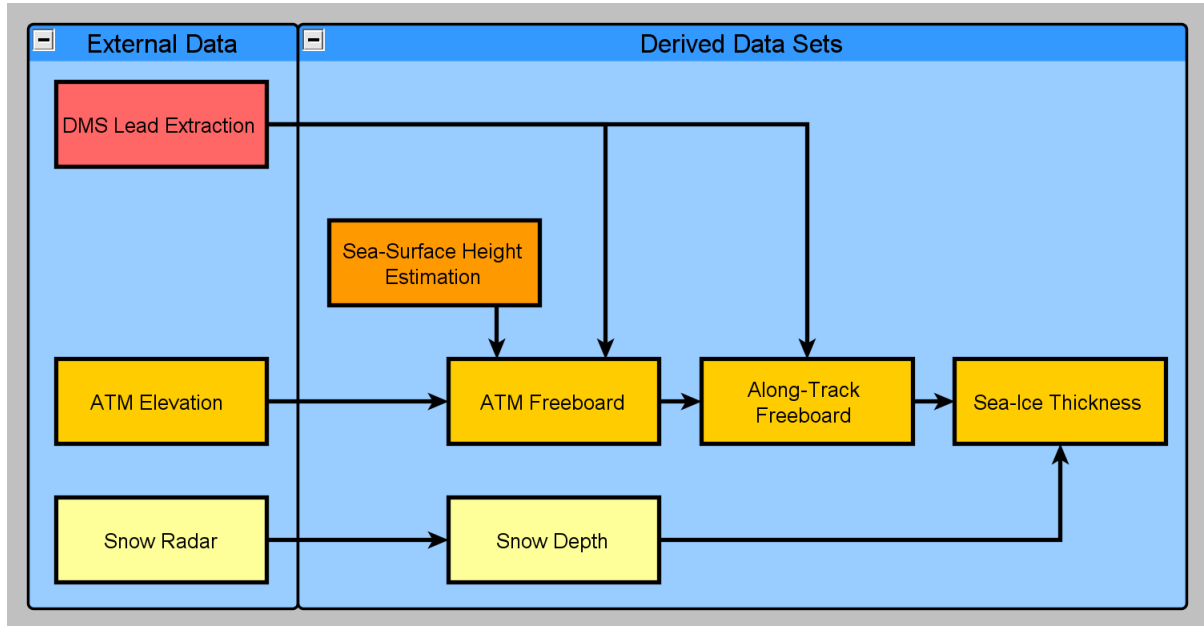


Figure 1: Organization flow chart of sea ice products.

implemented between the version 1 and version 2 data sets. Individual flight specific details are documented in the appendix.

2 Retrieval of sea ice freeboard

2.1 Freeboard and sea surface height parameters

The primary product given by laser altimeters is the surface elevation referenced to an ellipsoid, h_e . However, the more geophysically useful parameter we wish to retrieve from this product is the height of the snow plus ice surface above sea level, termed the freeboard, fb . The conversion of elevation data into sea ice freeboard is accomplished by subtracting out the instantaneous sea surface height h_{ssh} from each elevation measurement:

$$fb = h_e - h_{ssh} \quad (1)$$

| Parameter | Data source |
|----------------|---------------------------|
| h_{geoid} | EGM08 geoid |
| $h_{dynamic}$ | DTU10 Mean Sea Surface |
| h_{ocean} | TPX08.0 |
| h_{load} | TPX08.0 |
| h_{earth} | ATM processing (see text) |
| $h_{pressure}$ | MOG2D model, Meteo France |

Table 1: Sea surface height data sources.

The instantaneous sea surface height at a given point in space and time can be written as (*Chelton et al.*, 2001):

$$h_{ssh} = h_{geoid} + h_{dynamic} + h_{tides} + h_{pressure} \quad (2)$$

where h_{geoid} is the geoid, h_{tides} is the contribution of tidal forces, $h_{pressure}$ is the effect of atmospheric pressure loading, and $h_{dynamic}$ is the dynamic topography of the ocean surface. As a first step, we estimate the instantaneous sea surface height along the flight tracks through modeled estimates for the h_{geoid} , $h_{dynamic}$, h_{tides} , and $h_{pressure}$ terms. Data sources used in the initial estimation of the sea surface height terms are shown in Table 1.

The h_{geoid} component is taken from the EGM08 geoid, while the $h_{dynamic}$ component is estimated from the 1 minute by 1 minute DTU10 Mean Sea Surface data set (*Andersen and Knudsen*, 2009).

The h_{tides} component can be further decomposed into 4 terms:

$$h_{tides} = h_{ocean} + h_{load} + h_{earth} + h_{pole} \quad (3)$$

where h_{ocean} is the ocean tide, h_{load} is the load tide, h_{earth} is the solid earth tide, and h_{pole} is the pole tide.

The ATM elevation product is provided in the ITRF standard tide-free system where the solid earth tide has been removed. A standard latitude dependent correction for the permanent earth tide, $h_{permtide-corr}$, is applied to the data used here to place the data in a mean tide system relative to the WGS84 ellipsoid. The pole tide is a small amplitude ($< \sim 2$ cm), long wavelength tide component caused by oscillations in the

Earth’s rotation axis, it has not been included with this data set since its impact on freeboard determination should be minimal. The TPXO8.0 tide model is used to estimate the h_{ocean} and h_{load} components (*Egbert and Erofeeva, 2002*).

The classic expression for the $h_{pressure}$ component can be rewritten as:

$$h_{pressure} = \Delta P / (\rho_w g) \quad (4)$$

where ΔP is the difference between the surface air pressure at the local point from the instantaneous mean surface air pressure over the ocean, $\rho_w = 1024 \frac{kg}{m^3}$ the density of sea water, and $g = 9.8 \frac{m}{s^2}$ the gravitational acceleration. However, this represents only the time-invariant response of the sea surface height, we therefore use a dynamic atmospheric correction term taken from the MOG2D model (*Carrère and Lyard, 2003*) provided by Meteo France.

2.2 Sea surface height and freeboard determination

The previously described sea surface height parameters cannot be modeled with sufficient accuracy for the useful retrieval of freeboard given that centimeter level accuracy of the sea surface height is necessary for sea ice thickness studies. A combination of the modeled sea surface height with local sea surface height observations is thus required to achieve the desired centimeter level accuracy for the freeboard retrievals. A first step in the freeboard retrieval process is an initial removal of the modeled parameters affecting sea surface height from h_e , resulting in a corrected elevation h_{corr} :

$$h_{corr} = h_e - (h_{tides} + h_{geoid} + h_{dynamic} + h_{pressure}) \quad (5)$$

with the resulting freeboard then calculated as:

$$fb = h_{corr} - z_{ssh} \quad (6)$$

where z_{ssh} is the locally determined sea surface elevation with respect to the h_{corr} elevation data set, the determination of z_{ssh} at each point along the flight track follows from the retrieval of individual sea surface height observations described in detail below.

A set of sea surface elevation estimates, h_{tp} , are first found through extraction of the h_{corr} elevation data identified over leads in the IceBridge visible imagery data sets. For all but the Arctic 2009 data set (and other specific cases noted in the appendix), an automated lead detection algorithm called Sea Ice Lead Detection Algorithm using Minimal Signal (SILDAMS) (*Onana et al.*, 2013) which utilizes the geolocated IceBridge DMS imagery is used. SILDAMS applies a minimal signal transformation on DMS pixel brightness values to carry out a localization around low pixel intensities which correspond to lead areas. The transformed outputs are within a uniform dynamic variability over the set of numbers from $[0, 1]$ for a variety of input image pixel intensities. This allows specified thresholding of the transformed outputs to be set for the identification and classification of three different lead classes corresponding to open water areas, grease ice/nilas, and newly frozen leads with non-snow-covered grey ice (see Fig. 2). Each of these lead classes has an ice thickness less than 30 cm (*World Meteorological Organization*, 1970) and should thus have an elevation to within 3 cm of the local mean sea level making them suitable for use as sea surface tie points. To account for biases in the use of thin ice areas as sea surface tie points, we subtracted 0.005 m and 0.02 m of elevation for sea surface height determination using the ATM data over grease ice/nilas and grey ice, respectively. These values were chosen to correspond to expected freeboards of snow-free ice types defined by the World Meteorological Organization nomenclature.

For the 2009 Arctic campaign, leads and ice type were categorized through visual inspection of CAMBOT images (*Krabill*, 2009). Visual lead identification, rather than an automated approach using SILDAMS, was also used due to the complexity of the CAMBOT images caused by failure of the mechanical camera shutter and uneven image exposure in some portions of the images. The CAMBOT images are taken once every five seconds along each flight path using a Canon EOS DIGITAL REBEL XT_i camera. The images are time tagged and the geolocation of the center point, height of the aircraft above the surface, and aircraft heading are provided from the aircraft trajectory information based on the time tag. We have measured the angular resolution of the camera images using pictures of three distinct buildings over the Thule Airforce

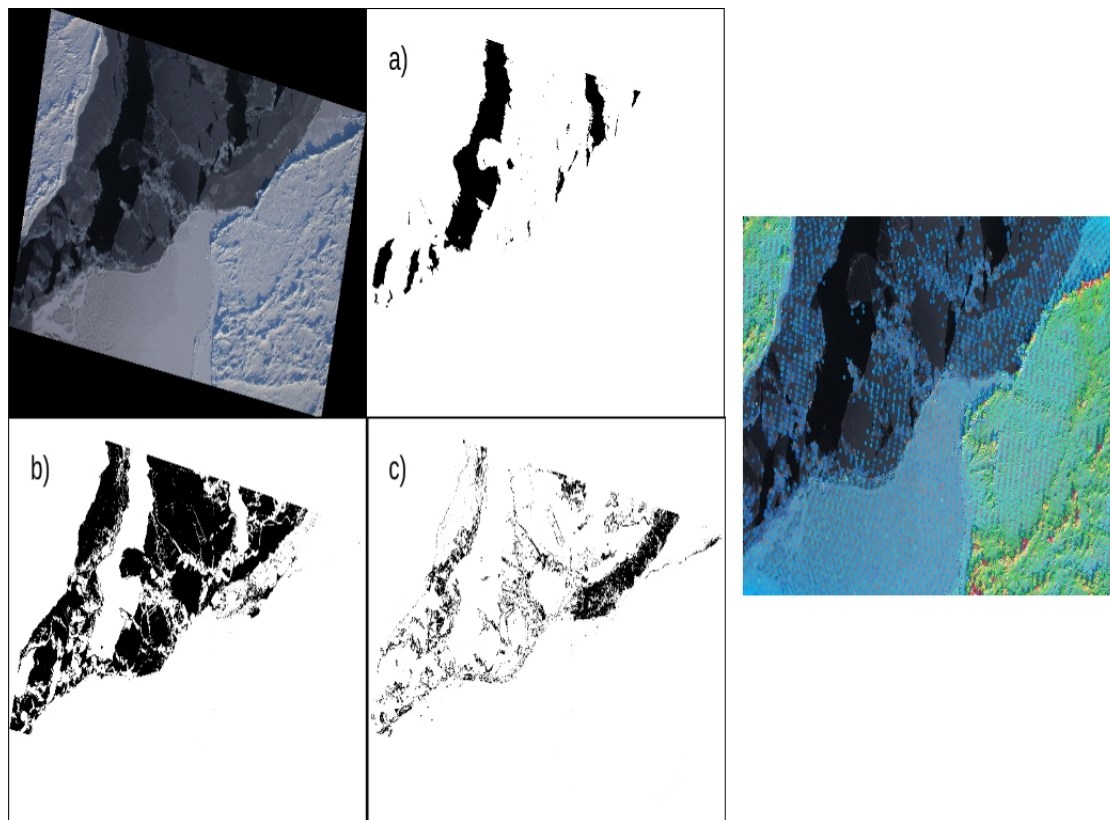


Figure 2: Example DMS image of sea ice with results from the SILDAMS algorithm displaying the ability to distinguish between a) open water leads b) nilas and grease ice and c) non-snow-covered grey-white ice. Overlain ATM elevation measurements (colored circles) are also shown. The colors correspond to height variations in the ATM data with cool colors (e.g. blue and purple) having a low elevation and warm colors (e.g. yellow and red) having a high elevation.

Base collected in 2009 with CAMBOT system and 2010 with the DMS system. The spatial size of the buildings were assumed to be unchanging and measured with the DMS imagery in 2010, combined with the known aircraft altitude from the CAMBOT system these same buildings were used to determine the angular resolution of the CAMBOT system to be $58.12^\circ \times 40.71^\circ$. The aircraft altitude and angular resolution were used to determine the pixel size for each CAMBOT image in the 2009 data set. The pixel size was combined with the image center point location, aircraft heading, and a standard coordinate rotation to geolocate the pixels of each CAMBOT image. However, the time tagging procedure for the CAMBOT data set was found to be typically valid only to within ± 1 second, which introduces geolocation errors for each image. To refine the geolocation of each image, we have constructed software to manually align each CAMBOT image. The software overlays the more accurately geolocated ATM elevation data (accurate to better than 1 m, *Schenk et al.*, 1999) onto each image, and then allows the operator to adjust the CAMBOT geolocation by manually changing the geolocation of the center point of each image. This was done until topographic features such as ridges and leads were found to match between the images and ATM data, see Figure 3 for an example image showing a manually aligned CAMBOT image with ATM data overlain. By matching the location of the leads in the visible imagery with those of the ATM h_{corr} elevations, the local sea surface elevation and freeboard of each ATM elevation point was retrieved in the same manner as leads identified with SILDAMS. Bias removal due to the use of thin ice types as sea surface reference points was done in the same manner as above using the SILDAMS output. The albedo dependence of ice type with thickness was found to impact the ATM data, very smooth specularly reflecting surfaces such as open water and thin ice covered leads caused a large loss in the number of returns from the ATM wide scan system. Non-snow covered thick grey-white ice had the largest number of returns which approached the sampling density of the surrounding snow-covered sea ice. Thus, even if leads are present in an area, the amount of sea surface elevation estimates may be much more limited in number than those from an equivalent area of returns over sea ice. In later campaigns, the smaller incidence angle of the ATM narrow scan instrument largely mitigates this issue.

The spatial resolutions of the ATM laser footprint and lead detection steps are ~ 1 m for the nominal flight altitude (460 m) of the IceBridge data set. To account for geolocation errors as well as the presence of mixed lead/sea ice data within the ATM returns, the requirement of a minimum 1 m lead buffer was set for each ATM return over a lead for it to be used as a sea surface estimate. This is necessary because mixed lead/sea

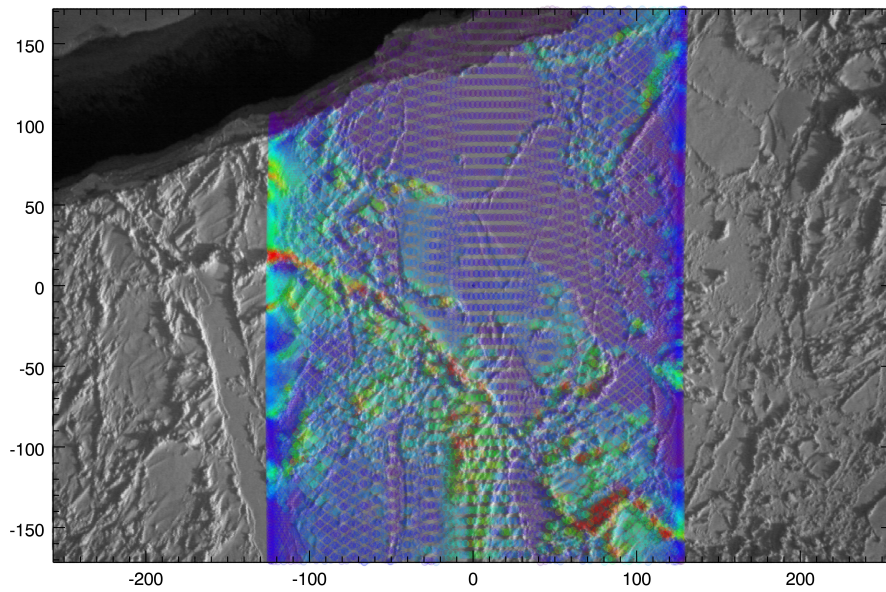


Figure 3: Example manually aligned CAMBOT image of sea ice with overlain ATM elevation measurements (colored circles) also shown. The colors correspond to height variations in the ATM data with cool colors (e.g. blue and purple) having a low elevation and warm colors (e.g. yellow and red) having a high elevation.

ice returns are prevalent due to the highly backscattering sea ice portion of the surface; as such, laser returns near the edge of a lead are not representative of the actual sea surface elevation but rather that of the sea ice within the laser footprint. Thus, the set of sea surface elevation estimates, h_{tp} , are taken from the h_{corr} elevation data set where leads are found, and the lead is found to extend at least 1 m in all directions beyond the center point.

Within a given area, \bar{h}_{tp} can be found from the set of sea surface elevation estimates, h_{tp} which were determined using the combined ATM and visible imagery lead detection method described previously. \bar{h}_{tp} is calculated using the following procedure: All values of h_{tp} within ± 250 m from the center point are first combined into a histogram with a 2 cm bin size. A value of ± 250 m has been chosen to span the width of an individual DMS or CAMBOT image. At minimum, we expect the local sea surface height to be constant over a length scale corresponding to the first mode baroclinic Rossby radius of deformation which is on the order of 10 km for latitudes greater than 60° (Chelton *et al.*, 1998). The Rossby radius is associated with the length scale at which oceanic eddies form, these eddies can cause local inhomogeneities in the sea surface height. An analysis of histograms of ATM elevations over known flat surfaces, including separate cases with open water and flat snow-covered sea ice (e.g. Farrell *et al.*, 2012), showed that the elevation distributions are Gaussian in shape with a minimum standard deviation of ~ 5 cm. For large leads during the 2012 and 2013 Arctic campaigns, the standard deviation of the ATM narrow swath instrument was $\sim 3-5$ cm which is of higher precision than the wide scan instrument which was used exclusively in the early part of the mission. We thus ideally expect the distribution of all h_{tp} points within the length scale defined by the Rossby radius to be similar in shape and width. However, a variety of error sources ranging from geolocation errors, misidentification of lead returns in the visible imagery, and errors in the h_{ssh} data sources lead to deviations from this ideal scenario. These errors also preclude the use of the mean value of h_{tp} and standard error analysis techniques from being used to determine \bar{h}_{tp} and its associated error. The misidentification of lead returns within the combined ATM and photography data causes the largest impact which, when present, can be seen as the presence of secondary and higher modes in the histogram of the h_{tp} points. In determining \bar{h}_{tp} , we wish to use the points corresponding to the mode with the lowest elevation. This is accomplished through the use of the centroid of a Gaussian fit function to the histogram of h_{tp} . The following conditions

have been imposed to determine whether the fitted Gaussian function is of a high enough quality for use in determining \bar{h}_{tp} :

$$\begin{cases} \sigma_{fit} \leq 0.11 \text{ m} \\ \chi^2 < 0.015 \\ N \geq 40 \end{cases} \quad (7)$$

where σ_{fit} is the standard deviation of the Gaussian fit, χ^2 is the reduced chi-square goodness-of-fit, and N is the number of h_{tp} points used to construct the histogram for the Gaussian fit. In cases where a multi-modal distribution of h_{tp} is observed, the above parameters will not be satisfied for the initial Gaussian fit. If this occurs, an iteration is then performed by discarding the largest h_{tp} elevation point in the set, performing another Gaussian fit, and retesting the fit parameters. The iteration is repeated until the conditions for the fit parameters are satisfied, at which point \bar{h}_{tp} is subsequently determined. If the conditions for the fit parameters are not met, then the sea surface height and freeboard are not calculated. See Figure 4(a) for an example of a case where the initial Gaussian fit parameters were satisfied on the first iteration, and Figure 4(b) for an example case of a multimodal distribution where the iteration produced a fit of the first mode only.

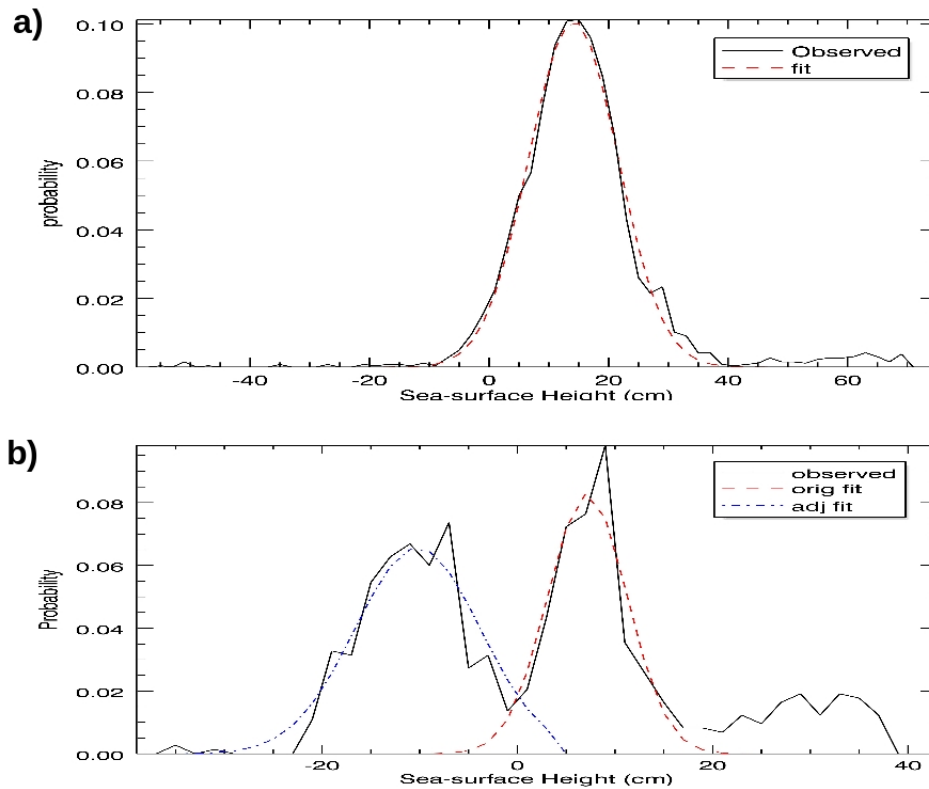


Figure 4: a) Gaussian fit to sea surface height data points which passed the quality requirements with no iteration required. b) Gaussian fit to sea surface height data points which passed the quality requirements after iterative removal of data points.

The previously described procedure produces a set of discrete sea surface height observations along the flight track. The availability of these sea surface height observations was found to be inconsistently available along each flight track due to ice conditions, in particular, few leads were found to occur in the compact multiyear ice areas of the Arctic. This creates uncertainties in the retrieval of freeboard since the quality of the sea surface height observations decreases with distance due to inaccuracies in the removal of the modeled sea surface height parameters shown in equation 2. Therefore, to construct the freeboard profiles along the flight track and determine the uncertainty of each data point (which is inherently variable along the flight path due to uneven lead spacing), the sea surface height along the full flight track was interpolated using

an ordinary kriging approach (e.g. *Cressie*, 1993). Since the sea surface height field is non-isotropic and non-homogeneous, we perform the interpolations over 200 km segments of each flight line and assume that the covariance of the sea surface height field is a homogeneous function of distance. Using these assumptions, the interpolation is then performed by minimizing the error variance of the interpolated vector of sea surface heights along the flight path. Briefly, this is done by solving the equation

$$z_{ssh} = \mathbf{W}^T \mathbf{z}_o \quad (8)$$

where z_{ssh} is the interpolated sea surface height at a specific point along the flight path, \mathbf{z}_o is the vector of observed sea surface height observations comprised of the set of \bar{h}_{tp} values calculated for each flight segment, and \mathbf{W} is the weight vector. \mathbf{W} is found by solving

$$\begin{pmatrix} W_1 \\ \vdots \\ W_n \\ \mu \end{pmatrix} = \begin{pmatrix} & & & 1 \\ & \mathbf{C} & & \vdots \\ & & & 1 \\ 1 & \dots & 1 & 0 \end{pmatrix}^{-1} \begin{pmatrix} C_{o1} \\ \vdots \\ C_{on} \\ 1 \end{pmatrix} \quad (9)$$

$$\mathbf{W} = \begin{pmatrix} W_1 \\ \vdots \\ W_n \end{pmatrix} \quad (10)$$

where \mathbf{C} is the covariance matrix and C_{oy} is the covariance between the interpolation point y , and the observation point o . The elements of the covariance matrix are assumed to be a homogeneous function of distance which is modeled as a Gaussian process with the respective elements taken to be

$$C_{xy} = \epsilon_{ssh}^2 + \sigma_z^2 \left(1 - e^{-\frac{d_{xy}^2}{L^2}} \right) \quad (11)$$

and

$$C_{on} = \left[\epsilon_{ssh}^2 + \sigma_z^2 \left(1 - e^{-\frac{d_{on}^2}{L^2}} \right) \right] e^{\left(\frac{-d_{on}}{L_m} \right)} \quad (12)$$

where d_{xy} is the distance between points x and y , d_{on} is the distance between observation points o and n , L is the correlation length of the sea surface height observations (\mathbf{z}_o) along the flight segment, L_m is the correlation length of the sea surface height measurements, σ_z is the standard deviation of the sea surface height observations, and ϵ_{ssh} is the uncertainty of the sea surface height observations. When a large number of closely spaced leads are present (which is typical in the Antarctic region) problems arise in the matrix inversion to determine the weights used in the sea surface height interpolation algorithm. To mitigate this, the \bar{h}_{tp} observations are averaged to 5 km to avoid singularities during the matrix inversion process when a potentially ill-conditioned matrix is detected in processing. Lastly, the method of *Deutsch*, [1996] is applied to correct for any non-physical negative weights and ensure unbiasedness.

From the previously described method for determining \bar{h}_{tp} containing at least 40 observations and a standard deviation of 0.11 m, the uncertainty for the sea surface height observations should theoretically be better than $0.11/\sqrt{40} = 0.017$ m. However, additional errors such as unresolved aircraft pitch and roll errors set will likely make this number higher since each sea surface height elevation data point, h_{tp} , is not statistically independent. We take $\epsilon_{ssh} = 0.058 / (\sum_{i=1}^n \exp(-\frac{d_{oi}^2}{L^2}))^{.5}$ meters (with a maximum value of $\epsilon_{ssh} = 0.058$ m) based on observations from the 2009 Arctic data set where 0.058 m is the standard deviation of the differences of all \bar{h}_{tp} measurements within ± 5 km (the Rossby radius where we expect the sea surface height to be constant) of each individually observed lead. Using a length scale smaller than ± 5 km did not change the maximum value of $\epsilon_{ssh} = 0.058$ m suggesting that this is the minimum uncertainty of a single sea surface height observation due to instrumental limitations. The higher precision of the narrow scan instrument will likely lead to a lower value for ϵ_{ssh} , but this has not been implemented at this time. Lastly, the sea ice freeboard is then determined by combining equations 6 and 8. The uncertainty in sea surface height and therefore freeboard at each point is given by

$$\sigma_{ssh} = \left[\left(\begin{array}{cccc} W_1 & \cdots & W_n & \mu \end{array} \right) \left(\begin{array}{c} C_{o1} \\ \vdots \\ C_{on} \\ 1 \end{array} \right) \right]^{\frac{1}{2}} \quad (13)$$

Qualitatively, the local sea surface height is determined by weighting the sea surface height observations as a function of distance, with nearby \bar{h}_{tp} points receiving the largest weight. The uncertainty decreases as the number of sea surface observations increases and the distance from each sea surface observation decreases, approaching $\sigma_{ssh} = \frac{0.058}{\sqrt{N}}$ meters in an area with many nearby sea surface height observations. The uncertainty approaches that of the background sea surface height field standard deviation, σ_z , as the distance from the nearest sea surface height observation becomes large.

2.3 Freeboard products

The method described previously is used to calculate the freeboard and its associated uncertainty at each individual ATM data point (~ 1 m spatial resolution) where the local sea surface height was determined. However, in order to combine the freeboard data with the snow depth estimates (described in the next section) for the retrieval of sea ice thickness, we place the high resolution freeboard estimates onto the same spatial resolution as the snow depth measurements. This is done by averaging the individual freeboard data to a 40 m resolution profile along the flight track centered over the snow radar footprints, thus the freeboard products are produced at a spatial resolution of 40 m. However, due to the loss of ATM data over surfaces with low backscatter towards the laser receiver (leads and non-snow covered thin ice as can be seen in Figures 2 and 3), an adjustment to the profile data is first needed to account for the undersampling of the freeboard of thin ice. This adjustment is performed by filling ATM data gaps using the SILDAMS output as a proxy freeboard data set. The freeboard of points corresponding to open water, f_{ow} were set to zero. The mean freeboard of points corresponding to “thin ice” in the SILDAMS algorithm were set to be $f_{ti} = 0.005$ m corresponding to the WMO freeboard (and ice thickness) for grease ice/nilas. Similarly, the points corresponding to the “grey ice” classification in the SILDAMS algorithm were set to be $f_{gi} = 0.02$ m. Based on these estimates,

we determine an adjusted average freeboard through the combined use of the ATM and SILDAMS freeboard outputs over a 40 m area. The ATM and SILDAMS data were placed on a 1 m resolution grid with the 40 m resolution adjusted freeboard, fb_{adj} , found using the following relation:

$$fb_{adj} = \frac{(n_{ow}f_{ow} + n_{ti}f_{ti} + n_{gi}f_{gi} + n_{ice}\bar{fb})}{(n_{ow} + n_{ti} + n_{gi} + n_{ice})} \quad (14)$$

where n_x corresponds to the number of open water, thin ice, grey ice, and sea ice grid points in the 40 m area detected by SILDAMS, and \bar{fb} is the mean freeboard from the ATM data within the area. This adjusted freeboard represents the profile of the mean freeboard along the IceBridge flight line where data gaps over low backscattering ice and water surfaces has been accounted for. A full list of the gridded freeboard and ancillary data products are listed in Table 2.

The methodology applied for the retrieval of freeboard is independent of location and thus is used to retrieve freeboard for both the Arctic and Antarctic IceBridge campaigns. However, for the 2009 Arctic campaign no DMS data were available for the automated identification of leads. CAMBOT data are available for all of the 2009 Arctic campaign with the exception of a portion of the April 5th flight where mechanical problems prevented photographs from being taken. Thus, freeboard retrievals were still done for the 2009 Arctic campaign, but these could only be processed to the point of the \bar{fb} level rather than to the more accurate fb_{adj} level.

3 Retrieval of snow depth

Snow depth is retrieved using the University of Kansas' snow radar (*Leuschen, 2009*). For the 2009 Arctic data set, snow depth is retrieved using the method described by *Kurtz and Farrell, [2011]*, while for subsequent campaigns the method follows that described in *Kurtz et al., [2013]*. Briefly, the retrieval algorithm detects the snow-air and snow-ice interfaces within the radar time domain signal and determine the snow depth by multiplying by the speed of light within the snow pack. The snow-ice interface was set to be the highest peak in the radar signal while the snow-air interface was determined using a combined peak and threshold

method. However, modifications to the radar configuration between IceBridge campaigns (e.g. antenna design and placement) precludes the use of the previously used algorithms from being applied to the 2010 data. Specifically, the signal-to-noise ratio was much lower in 2009 and required that the algorithm be designed to identify returns near the noise threshold. For the 2010 data set, the signal-to-noise ratio was increased through changes to the radar design, however this means that modifications to the algorithm needed to be done for the retrieval of snow depth. To account for these changes in the radar configuration, for the 2010 and later campaigns we base the detection thresholds for the air-snow interface on the relative radar return power. We use the 2009 radar data set as the basis for the algorithm changes since the in-situ study of *Farrell et al.*, [2012] was carried out during this time and gives us a reference with which we initially determined known return power values for the snow-air and snow-ice interfaces. The location of the snow-ice interface is still determined as the largest maxima in the radar signal below the air-snow interface. The return power in dB is calculated here as $P = 10 * \log_{10} \left(\frac{m_{data}}{N_{echo}} \right)$ where m_{data} is the magnitude of the echogram data array and N_{echo} is the number of points in the vertical direction of the echogram file. To improve the signal-to-noise ratio and reduce the possibility of radar speckle from being misidentified as an interface layer, the return power data were first incoherently averaged over 40 points corresponding to a length scale of ~ 40 m.

The return power values for the snow-air interfaces identified in the 2009 data set were found to vary between $P_{s-a}^{min} = -4.0$ dB, and $P_{s-a}^{max} = -0.5$ dB with a mean value of $P_{s-a}^{mean} = -2.3$ dB, these conditions are used here to locate the snow-air interfaces in the 2010 data set. However, the data from the snow radar are presently not radiometrically calibrated and thus vary based on the parameters of the instrumentation, the flight parameters, and the processing methodologies used to create the final data values. While a simplification of the return power behavior for the FMCW radar used here, the standard radar equation for a pulse-limited altimeter (*Raney, 1998*) outlines the basic set of parameters which influence the final data value

$$P_r = \frac{P_t G^2 \lambda^2 \sigma^0 \pi c \tau T_{BP}}{(4\pi)^3 R^3} \quad (15)$$

where P_r is the received power, P_t is the transmit power, G is the antenna gain, λ the wavelength,, σ^0 the scattering coefficient, τ is the pulse length, T_{BP} is the range time bandwidth product, and R the range to the target. Instrumentation changes have led to variations in these parameters on for each IceBridge campaign.

Flight considerations also play a role, for example R is generally equal to the nominal IceBridge flight altitude of 460 m, but can be as low as 240 m as the aircraft altitude is varied to fly under clouds which negatively impact the laser altimetry data. A calibration adjustment for each individual radar echogram is therefore necessary to determine the final threshold power range where we expect the snow-air interface to be located.

First, we define scale, m , and offset, b , parameters which are determined for each echogram by simultaneously solving

$$y_1 = mx_1 + b \quad (16)$$

$$y_2 = mx_2 + b \quad (17)$$

where $y_1 = 2.25$ dB which is the average power of the snow-ice interface observed in the 2009 Arctic data set, x_1 is the average power of the snow-ice interface for the desired radar echogram, $y_2 = -5.0$ dB which is the average power of the first 100 bins located at least 5 m above the point of maximum power in the 2009 Arctic data set, and x_2 is the average power of the first 100 bins located at least 5 m above the point of maximum power for the desired radar echogram. We here define the maximum power of the adjusted snow-air interface to be $\hat{P}_{s-a}^{max} = mP_{s-a}^{max} + b$, similarly the minimum power for the adjusted snow-air interface is defined to be $\hat{P}_{s-a}^{min} = mP_{s-a}^{min} + b$. These conditions determine the region of the radar return where we expect the snow-air interface to be located. The search for the snow-air interface thus occurs when the return power level, P_{s-a} , for the snow-air interface satisfies the following requirements:

$$P_{s-a} \geq \hat{P}_{s-a}^{min} \quad (18)$$

$$\overline{P_{s-a}} \geq \hat{P}_{s-a}^{min} \quad (19)$$

where $\overline{P_{s-a}}$ is the mean power in the six range bins that follow the \hat{P}_{s-a}^{min} . Once these conditions are satisfied the snow-air interface is defined following the observations described by *Farrell et al.*, [2012] to be either the location of the first local maxima in the return or the leading edge of the radar signal. The snow-air interface is thus defined here as the first point where one of the following conditions is satisfied:

1. The leading edge of the radar return from the snow-air interface is found. The leading edge is defined here as the point where the radar return power begins to continuously increase (i.e. $\frac{\partial P}{\partial x} > 0$) until the maximum snow-air interface power, \hat{P}_{s-a}^{max} is reached.
2. If a local maxima occurs greater than $mP_{s-a}^{mean} + b$ and σ above the adjacent points (to eliminate random noise from being misidentified as a maxima), where σ is the standard deviation of the radar noise level, then this point is chose as the snow-air interface location.

An iteration of the above method is then performed by rescaling the threshold power values: y_1 is set equal to the mean echogram power for the snow-air interface and $y_2 = P_{s-a}^{mean}$. The first iteration provides an approximation for the parameters m and b by scaling the return power values by the snow-ice interface power and the radar noise, however changes to the snow radar system have reduced the noise level in successive campaigns. The second iteration scales the return power values to the snow-air interface allowing for more accurate estimates of m and b to be made.

The snow depth is then found by differencing the snow-air and snow-ice interfaces in the time domain and multiplying this difference by the speed of light within the snow pack, c_{snow} . The speed of light in the snow pack was taken to follow the relation between snow density and dielectric constant given by *Tiuri et al.* [1984] as

$$\epsilon_d = 1 + 2\rho_s \tag{20}$$

$$c_{snow} = \frac{c}{\sqrt{\epsilon_d}} \tag{21}$$

where c is the speed of light in vacuum and ρ_s is the snow density (in $\frac{g}{cm^3}$). The snow density was taken to be $320 \frac{kg}{m^3}$ following the climatological mean snow density of *Warren et al.*, [1999]. Once the snow-air and snow-ice interfaces were identified, we applied a locally weighted robust linear regression at a 40 m length scale to reduce the impact of outliers in the final determination of the snow-air and snow-ice interface locations. This effectively reduces the resolution of the retrieved snow depths to 40 m.

As described in *Kurtz and Farrell*, [2011], the behavior of the radar over leads and the apex of steep pressure ridges must also be accounted for in the snow depth retrieval method. Lead areas were flagged using the method described in *Kurtz and Farrell*, [2011] and the snow depth was set to zero to correspond to the negligible snow cover on open water and newly frozen leads. We also discard data where the signal is too low for the retrieval of snow depth. Based on the analysis of coincident laser data from the ATM to identify ridge locations, the conditions for discarding the data due to insufficient signal strength were set to be:

$$P_{s-i} \geq -1.5m + b dB \quad (22)$$

$$\overline{P_{s-i}} \geq -1.5m + b dB \quad (23)$$

where $\overline{P_{s-i}}$ is the mean power in the three range bins that follow the snow-ice interface. Discarding of data due to insufficient signal strength occurred for 16% of the snow depth observations for the 2009 Arctic campaign, but will be variable for each campaign due to flight line and instrumentation differences.

An additional quality control step for the retrieved snow depths is also necessary to discard data collected when warm surface temperatures are present. *Kurtz and Farrell*, [2011] found that warm surface temperatures led to anomalously low snow depth values due to the changing dielectric properties of the snow pack. Similar to the study of *Kurtz and Farrell*, [2011], we discard data when the surface temperature is greater than -5 °C. When available, the surface temperature is determined from the IceBridge KT-19 infrared radiation pyrometer data set (*Shetter et al.*, 2010). When instrumental observations are unavailable, we use the thermodynamic sea ice model of *Kurtz et al.*, [2011] forced with ECMWF meteorological data to determine the surface temperature.

The snow depth retrieval method outlined here is essentially empirical, an updated method which utilizes known physics of the radar return is underway. It will be evaluated and included in a future version of the data product if it shows an improvement over the current method.

4 Sea ice thickness

4.1 Thickness determination and spatial resolution

Sea ice thickness, h_i , is calculated using the previously described freeboard and snow depth data sets and the hydrostatic balance equation:

$$h_i = \frac{\rho_w}{\rho_w - \rho_i} f b_{adj} - \frac{\rho_w - \rho_s}{\rho_w - \rho_i} h_s \quad (24)$$

where $f b_{adj}$ is the freeboard, h_s is the snow depth, ρ_w is the density of sea water, ρ_i is the density of sea ice, and ρ_s is the density of snow. ρ_w and ρ_i are taken to be $1024 \frac{kg}{m^3}$ and $915 \frac{kg}{m^3}$ which are derived from the result of field measurements summarized by *Wadhams et al.* [1992]. ρ_s is taken to be $320 \frac{kg}{m^3}$ following the climatological values compiled by *Warren et al.* [1999].

4.2 Error analysis

The error in the sea ice thickness retrieval (excluding the negligible contribution of errors due to variations in sea water density as shown by *Kwok and Cunningham*, 2008) can be written as

$$\sigma_{h_i} = \left[\left(\frac{\rho_w}{\rho_w - \rho_i} \right)^2 \sigma_{h_f}^2 + \left(\frac{\rho_s - \rho_w}{\rho_w - \rho_i} \right)^2 \sigma_{h_s}^2 + \left(\frac{h_s (\rho_s - \rho_w) + h_f \rho_w}{(\rho_w - \rho_i)^2} \right)^2 \sigma_{\rho_i}^2 + \left(\frac{h_s}{\rho_w - \rho_i} \right)^2 \sigma_{\rho_s}^2 \right]^{\frac{1}{2}} \quad (25)$$

where σ_{h_i} , σ_{h_f} , σ_{h_s} , σ_{ρ_s} , and σ_{ρ_i} are the uncertainties of the ice thickness, freeboard, snow depth, and densities of snow and ice, respectively. Density uncertainties are taken from previous in-situ measurements

described in the literature: σ_{ρ_s} is estimated to be 100 kg/m^3 based on the variability of ρ_s in the climatology of *Warren et al.* [1999], σ_{ρ_i} is estimated here to be 10 kg/m^3 which represents the expected range of densities for sea ice between 0.3 and 3 m thick (*Kovacs, 1996*). The uncertainty in the freeboard retrieval, σ_{h_f} , is variable along the flight path as described in Section 2. The snow depth uncertainty is not well known at this time. Uncertainty in the snow depth occurs due to a variety of factors including the finite range resolution of the radar, density uncertainties, and uncertainty in the detection of the snow-air and snow-ice interfaces. For the purposes of this study, we estimate the uncertainty using the difference between the IceBridge data and in-situ snow depth described in the study by *Farrell et al.*, [2012]. The mean difference between the survey and IceBridge data set was 0.8 cm, and there were 50 observations (40 m for each observation over a 2 km survey line). Assuming the method is unbiased the error is calculated as $\sigma_{h_s} 0.8 * \sqrt{50} = 5.7 \text{ cm}$, a recent study by *Webster et al.*, [2014] found an RMSE of 5.8 cm in comparison to in-situ data. However, we await further refinement of this uncertainty value with the addition of future in-situ comparisons. The uncertainty in ice thickness is then calculated using equation 25, with the uncertainties for the variable described above. The sea ice thickness uncertainty is thus a variable quantity, in particular due to the variable uncertainty in the freeboard retrievals.

5 Data products description

The full suite of data products and ancillary data sets are listed in Table 2. Additional ancillary data have been included for further analysis of the IceBridge data sets. These include the surface roughness, transmit and received signal strength of the ATM, and the KT19 surface and internal temperatures. A flag for ice type is also included for the Arctic region, the ice type flag data are taken from the nearest grid data on ice type from the Norwegian Met. Service OSI SAF system (<http://www.osi-saf.org/>). The gridded data products contain invalid data which are set to a value of -999, additionally, ice type data with a confidence level less than 50% were also set to -999.

| Name | Symbol in text | Description | Units |
|-------------------------------|---------------------|--|---------|
| Profile data | | | |
| Latitude | - | Latitude of the center grid point | Degrees |
| Longitude | - | Longitude of the center grid point | Degrees |
| Mean freeboard | $\bar{f}b$ | Mean freeboard (40 m resolution) of the ATM data only | m |
| Adjusted mean freeboard | $f_{b_{adj}}$ | Mean freeboard (40 m resolution) from the combined ATM-DMS data set | m |
| ATM points | n_{atm} | Number of ATM points in the 40 m grid | # |
| Percentage open water | p_{ow} | Percentage of open water in the 40 m grid | % |
| Percentage thin ice | p_{ti} | Percentage of thin ice in the 40 m grid | % |
| Percentage grey ice | p_{gi} | Percentage of grey ice in the 40 m grid | % |
| Freeboard uncertainty | σ_{ssh} | Uncertainty in the derived freeboard | m |
| Mean snow depth | h_s | Mean snow depth (40 m resolution) from the snow radar data set | m |
| Snow depth uncertainty | σ_{h_s} | Uncertainty in the derived snow depth | m |
| Sea ice thickness | h_i | Mean sea ice thickness (40 m resolution) | m |
| Sea ice thickness uncertainty | σ_{h_i} | Uncertainty in the derived sea ice thickness | m |
| Surface roughness | - | Standard deviation of the ATM elevation points in the 40 m grid | m |
| Transmit energy | - | Mean transmit signal strength (40 m resolution) of the ATM data | - |
| Received energy | - | Mean receive signal strength (40 m resolution) of the ATM data | - |
| Low energy correction | - | Correction added to the ATM elevation data for low signal strength | m |
| Scan angle correction | - | Correction added to the ATM elevation data for scan angle biases | m |
| Snow-air interface | - | Height of radar derived snow-air interface relative to the WGS84 ellipsoid | m |
| Snow-ice interface | - | Height of radar derived snow-ice interface relative to the WGS84 ellipsoid | m |
| Ice type flag | - | Flag for ice type, 0: first year ice, 1: multiyear ice | - |
| Ancillary data | | | |
| Corrected elevation | h_{corr} | Elevation with the modeled sea surface height parameters removed | m |
| Elevation | h_e | Original ATM elevation | m |
| Date | - | Date of measurement in YYYYMMDD | |
| Elapsed time | - | Time from start of day of the flight, in UTC | Seconds |
| Ellipsoid correction | h_e | Conversion factor between the WGS-84 ellipsoid and the Topex/Poseidon ellipsoid | m |
| Atmospheric loading | $h_{pressure}$ | Atmospheric pressure loading term for the sea surface height | m |
| Mean sea surface | - | DTU10 mean sea surface height equal to $h_{geoid} + h_{dynamic}$ | m |
| Ocean tide | h_{ocean} | Ocean tide term for the sea surface height | m |
| Load tide | h_{load} | Load tide term for the sea surface height | m |
| Permanent tide correction | $h_{permtide-corr}$ | Tide correction term used to place the data in the mean tide system | m |
| Total tides | h_{tides} | Sum of the ocean, load, and earth tide correction terms | m |
| Sea surface height | z_{ssh} | Local sea surface elevation with the ocean, load, and earth tide correction terms applied | m |
| SSH number | n_{ssh} | Number of ATM points used to determine the nearest \bar{h}_{tp} data point | # |
| SSH standard deviation | σ_{ssh} | Standard deviation of the Gaussian fit used to determine the nearest \bar{h}_{tp} point | m |
| SSH difference | - | Difference between centroids of the first and final Gaussian fits used to determine \bar{h}_{tp} | m |
| SSH elapsed time | - | Elapsed time since the last sea surface tie point was encountered | Seconds |
| SSH tie point distance | - | Distance to the nearest sea surface height tie point | m |
| File name | - | Name of the file from which the laser altimetry data were from | |
| Surface temperature | - | Surface temperature from the KT19 instrument | °C |
| KT19 internal temperature | - | Internal temperature of the KT19 instrument | °C |

Table 2: Descriptions of the final gridded freeboard, snow depth, and ice thickness output fields and ancillary data.

6 Ancillary data sets and adjustments

6.0.1 KT-19 surface temperature retrievals

A KT-19 infrared pyrometer is present on many of the campaigns to measure surface temperature. The data are recorded using an averaging rate, kt_{avg} , which has varied between 1-10 Hz for individual campaigns. At the nominal aircraft speed of $v_{aircraft} = 460$ km/hr (128 m/s), the averaging length is $a_l = \frac{v_{aircraft}}{kt_{avg}}$ which is one component of determining the footprint size. The two degree instrument field of view yields a footprint size of $f_{kt} = 15$ m at the nominal flight altitude of 457 meters. The footprint size of the recorded measurement is thus $a_l + f_{kt}$. The geolocation of the data are referenced to a GPS antenna located near the KT19 instrument. Meter to decameter level geolocation uncertainties may be present due to the lack of knowledge of the instrument pointing angle (assumed to be at nadir) as well as timing offsets from the instrument data system.

The uncertainty in the surface temperature retrievals are calculated following the KT19 product manual as

$$\sigma_{kt19} = 0.5 + 0.007\Delta T \quad (26)$$

where ΔT is the temperature difference between the target surface and the housing temperature, unmodeled uncertainties include surface emissivity variations, instrument issues, and atmospheric losses from clouds, fog, and atmospheric water vapor.

Prior to 2011 the response time setting for the emissivity for the KT-19 instrument was set at 1.0. However, published values for the emissivity of snow and sea ice are ~ 0.97 , a setting which was adopted for all Arctic and Antarctic campaigns beginning in 2012. A bias correction can be calculated by integrating Planck's law over the wavelength range of the KT19 instrument to determine the total intensity, I_1 , for the recorded temperature with emissivity, $\epsilon_1 = 1$, and the total intensity, I_2 , with emissivity, $\epsilon_2 = 0.97$:

$$I_1 = \int_{\lambda_1}^{\lambda_2} \frac{\epsilon_1 2hc^2}{\lambda^5} \frac{1}{e^{\frac{hc}{\lambda k_b T_1}} - 1} d\lambda \quad (27)$$

$$I_2 = \int_{\lambda_1}^{\lambda_2} \frac{\epsilon_2 2hc^2}{\lambda^5} \frac{1}{e^{\frac{hc}{\lambda k_b T_2}} - 1} d\lambda \quad (28)$$

where $\lambda_1 = 9.6 \times 10^{-6} \text{ m}$, $\lambda_2 = 11.5 \times 10^{-6} \text{ m}$, h is the Planck constant, c is the speed of light, k_b is the Boltzmann constant, T_1 is the temperature which was recorded using the KT19 sensor, and T_2 is the temperature of the surface with emissivity ϵ_2 . This equation does not have a closed form solution and must be solved numerically. Setting $I_1 = I_2$, the equation can be iteratively solved to determine T_2 . A plot of calculated values for $T_2 - T_1$ for different recorded KT19 temperatures, T_1 , is shown in Figure 5. A linear fit to the calculated values to determine the temperature bias is:

$$T_2 - T_1 = T_1 * 0.01066 - 1.263 \quad (29)$$

Equation 29 was used to correct the recorded KT19 temperature values to coincide with a surface emissivity of 0.97 for all data reported in the products prior to 2012.

6.0.2 Iceberg filter

The goal of the IceBridge sea ice campaigns is to measure the freeboard and thickness of sea ice. In the Antarctic region there are a substantial number of icebergs which contaminate the measurements of sea ice. Since the fundamental goal of the data provided in these products is to provide information on sea ice, we wish to filter out data which contain icebergs. Since icebergs cast long and dark shadows which can be mistaken for leads in the lead identification step using SILDAMS, we also wish to filter out these points. The following steps describe the process whereby the ATM data with iceberg contamination are identified and removed.

First, an ATM point cloud (anywhere from a small ~200m in length subset to an entire flight) is input into a function and a structure of two arrays are output. The first array (“iceberg”) contains the index of the points that are identified as being on the iceberg. The second array contains these iceberg indices, as well as those points lying within a specified radius from the edge of the iceberg (“shadow”); this additional buffer is

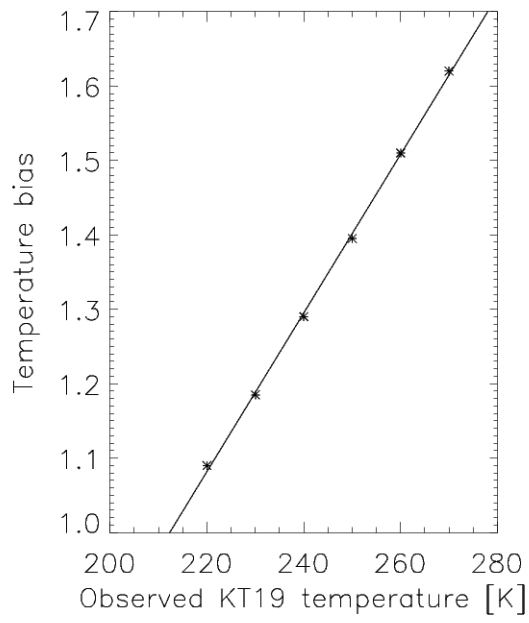


Figure 5: Starred points are calculated values for $T_2 - T_1$ for different recorded KT19 temperatures, T_1 . A linear fit to the data (solid line) which was used to calculate the temperature bias is given in equation 29.

an attempt to capture all the points that may be within the reach of a shadow cast from the iceberg. This “shadow” array is useful in conjunction with additional lead identification methods to differentiate areas identified as leads that are actual leads from those that are shadows. Tall icebergs with low sun angles often necessitate a large buffer to be used.

1. Projecting the input data

- (a) ATM data is first projected into a polar stereographic projection with a decameter resolution.
- (b) Next the projection is translated such that the minimum x and y values are set as zero; all other x and y values subsequently become positive.

2. Gridding the data

- (a) Two empty grids are created, spanning the entire range of x and y values. Grid A will contain the average value of all the points that fall within each grid square. Grid B will contain the maximum value of all the points that fall within each grid square.
- (b) Each point is then placed into the appropriate grid square based on its projected coordinates. Grid B values (maximums) are calculated instantly using logical operators whereas Grid A values (averages) are summed throughout the process and divided by the number of entries in each grid at the end.

3. Differentiating between icebergs and pressure ridges

- (a) Grid A (Average) values are used to identify the “tops” of icebergs, as pressure ridges may have a maximum value equal to or greater than icebergs, their 10 meter mean value will likely be much lower. As such Grid A squares with a value of 2.5 meters or greater (above the lowest ATM elevation data point) are identified as icebergs. Through visual identification using DMS imagery, this value of 2.5 meters was found during the three IceBridge 2009 Antarctic campaign sea ice flights to successfully identify all large icebergs while excluding all pressure ridges. All other icebergs below the 2.5 meter threshold (often just growlers) were assumed to be of negligible consequence to the calculation of areal ice thickness averages.

- (b) Grid A squares with an average value less than 2.5 meters are identified as level ice.
- (c) If no Grid A squares are found to be above 2.5 meters, the function simply returns a value identifying the presence of no significant icebergs.

4. Growing Iceberg regions

- (a) From our initial iceberg classification, we “grow” each iceberg grid square spatially, continuing to classify neighboring grid squares until a certain threshold is met. In this case, if the neighboring grid square’s value is greater than the mean of the level ice plus twice the standard deviation of the level ice, it is included as an iceberg.
- (b) The locations of icebergs identified from Grid A grid squares are the starting classification and Grid B is the grid upon which this threshold is calculated from to either continue or stop the iceberg region from growing. We use Grid A as a starting point in order to differentiate between icebergs and ridges, however we use Grid B to decide when to stop spatially growing as we would rather misidentify sea ice as an iceberg than miss an iceberg grid square.
- (c) The IDL “REGION_GROW” function is used to perform this task. An additional one grid point buffer is added around each iceberg through the use of the IDL SHIFT function to ensure all iceberg edges are identified.

5. Identifying iceberg shadows

- (a) Shadowed regions are calculated simply by adding an additional four grid squares around the entire selected iceberg region through the use of the IDL SHIFT function.

Selected indices identifying iceberg and shadow regions are added to a structure and returned to the main function. Iceberg data are not used in the calculation of freeboard, while data from the shadow filtered region are not used in the determination of sea surface height. An example of the iceberg filter using ATM elevation data overlaid on DMS imagery is shown in Figure 6.

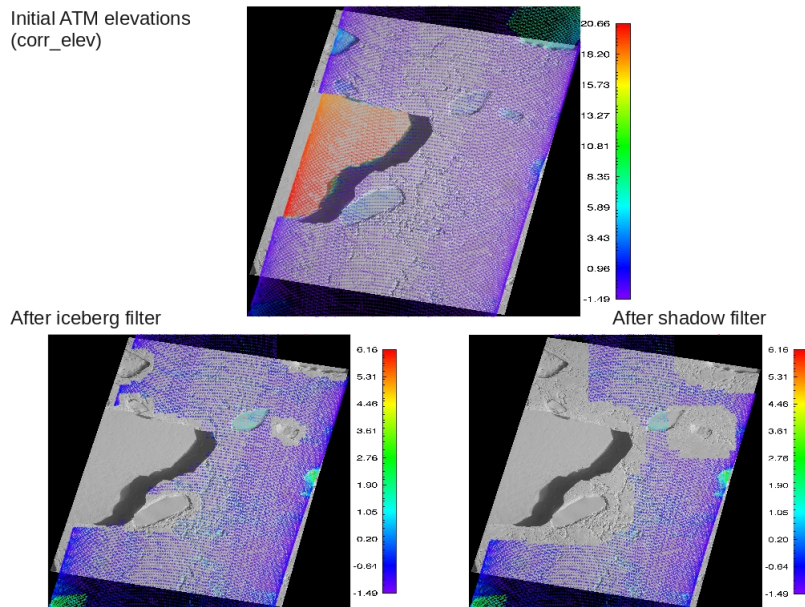


Figure 6: Visual representation of the iceberg filter. The image color bars refer to the corrected ATM elevations (corr_elev).

7 Version 2 changes

This section documents the changes which were made between the version 1 and version 2 data sets. Some changes were made prior to the release of the version 2 data set, but here all changes have been uniformly implemented to all campaigns.

7.1 Input improvements

This section describes changes to input data sets which improved the quality and consistency of the final data products.

7.1.1 Tide model update

The TPXO6.2 tide model has been updated to a newer version, the TPXO8.0 tide model which is used to estimate the h_{ocean} and h_{load} components. If all sea surface height corrections contained no error, then the standard deviation of the h_{corr} values would be equivalent to the instrument noise. We therefore expect that the standard deviation of the observed sea surface heights, \mathbf{z}_o , is a useful metric for determining whether the new tide model represents an improvement over the previous model. Table 3 shows the standard deviation of the set of sea surface heights for each flight line which have been averaged over individual campaigns. For the Arctic, the TPXO8.0 model performs at a slightly worse, though overall quite comparable level to the TPXO6.2 model. For the Antarctic region, the TPXO8.0 provides a noticeable improvement.

| | TPXO6.2 | TPXO8.0 |
|----------------|---------|---------|
| Arctic 2010 | 0.163 m | 0.169 m |
| Arctic 2011 | 0.137 m | 0.140 m |
| Arctic 2012 | 0.161 m | 0.161 m |
| Antarctic 2009 | 0.203 m | 0.185 m |
| Antarctic 2010 | 0.190 m | 0.170 m |

Table 3: Standard deviation of observed sea surface heights averaged by campaign using the TPXO6.2 and TPXO8.0 tide models.

7.1.2 Mean sea surface update

The h_{geoid} correction has now been replaced with the DTU10 Mean Sea Surface height, which is the sum of the EGM08 geoid and $h_{dynamic}$ components. In a similar manner to the tide comparison, we expect the standard deviation of elevation measurements to be lower if the new data set represents an improvement. Here, we use the standard deviation of all 40 m average elevation measurements for a given flight, not just lead points, and average them to determine a value for each campaign. These values are shown in Table 4. For both the Arctic and Antarctic regions, the DTU10 MSS offers a noticeable improvement.

| | EGM08 | DTU10 MSS |
|----------------|---------|-----------|
| Arctic 2009 | 0.431 m | 0.368 m |
| Arctic 2010 | 0.273 m | 0.240 m |
| Arctic 2011 | 0.212 m | 0.203 m |
| Arctic 2012 | 0.267 m | 0.245 m |
| Antarctic 2009 | 0.348 m | 0.334 m |
| Antarctic 2010 | 0.360 m | 0.333 m |

Table 4: Standard deviation of elevations averaged by campaign using the EGM08 and DTU10 corrections.

7.1.3 Dynamic atmospheric correction update

The atmospheric load, $h_{pressure}$, was previously taken assuming an isostatic response to surface pressure fields from ECMWF reanalysis data, it was referenced to the global mean surface pressure rather than the surface pressure over the ocean. This has been replaced by a new dynamic atmospheric correction term taken from the MOG2D model (Carrère and Lyard, 2003) provided by Meteo France. Table 5 shows the standard deviation of the set of sea surface heights for each flight line which have been averaged over individual campaigns. For the Arctic, the MOG2D model generally performs at a slightly better, though overall quite comparable level to the ECMWF inverse barometer correction. For the Antarctic region, the MOG2D model provides a distinct improvement.

| | ECMWF | MOG2D |
|----------------|---------|---------|
| Arctic 2010 | 0.159 m | 0.150 m |
| Arctic 2011 | 0.142 m | 0.153 m |
| Arctic 2012 | 0.159 m | 0.161 m |
| Antarctic 2009 | 0.407 m | 0.431 m |
| Antarctic 2010 | 0.667 m | 0.670 m |

Table 5: Standard deviation of observed sea surface heights averaged by campaign using the surface pressure inverse barometer correction from ECMWF reanalysis data, and the MOG2D model.

7.1.4 Land mask update

The previous version of the product manually edited out land data using a combination of mapping software and the DMS images. The land mask is now based on a combination of bathymetric and coastline data sets.

First, a bathymetric model produced by the Technical University of Denmark, National Space Institute (*Andersen et al.*, 2008; see http://www.space.dtu.dk/english/Research/Scientific_data_and_models for more information) is used to determine an initial set of land points. The bathymetric model has a one minute by one minute resolution. For each data point, if all of the four closest bathymetric model grid points are above the threshold of +10 meters, the point is flagged as land. Also for each query point, if any of the four closest bathymetric model grid points are above the threshold of -10 meters, and not already flagged as land, the query point is flagged as possible land. Next, the points flagged as possible land are compared to a set of coastline shapefiles to determine if the points are actually over land or water; this step is much slower than the method using the bathymetric model, but is much more accurate. The coastline shapefiles used were created by the NOAA National Geophysical Data Center and is in the GSHHG (A Global Self-consistent, Hierarchical, High-resolution Geography) dataset, Version 2.3.2, released August 1, 2014 (see <http://www.ngdc.noaa.gov/mgg/shorelines/gshhs.html> for more information). The full resolution version of the data are used in the land mask, and all data points determined to be over land are removed from further processing.

7.1.5 Ice type data set

Due to the failure of the AMSR-E instrument in 2011, ice type data was taken from the Norwegian Met. Service OSI-SAF system in subsequent campaigns. To maintain data consistency, we now use ice type data from OSI-SAF for all Arctic campaigns.

7.1.6 Combined ATM narrow and wide-swath data sets

During the initial generation of the Version 1 product, there were a number of data gaps in the final 40 m thickness/freeboard portion of the product for years using only narrow-scan ATM data (this covers most flights beginning in 2011). These are due to combination of factors such as missing ATM/DMS data coverage, a lack of nearby leads for accurate determination of a local sea-surface, or modeled ssh values outside allowable thresholds. Upon further investigation during reprocessing we found that much of this was due to the ATM narrow-scan lidar being more sensitive to aircraft roll than the ATM wide-scan lidar. Subsequently, even

during normal aircraft operation the ATM narrow-swath coverage would often completely leave the prescribed product reference point which was within 40 m of the nadir direction, this resulted in missing freeboard and thickness values in the final product. To alleviate this coverage issue, while still maintaining the benefits gained by using the ATM narrow-scan lidar, we have now combined the ATM narrow and wide-scan lidars.

As each lidar is independently controlled, coverage and filenames differ. Thus the first step in combining wide and narrow-scan data streams is to generate new filenames, based upon both data sets, with the first file starting at the timestamp of the first wide or narrow scan point. Each subsequent combined file is 400 seconds long (the approximate length of most uncombined ATM files) and contains any wide or narrow scan data within that time period; as such, ATM filenames reported in the final product will not match those at NSIDC for instances when data is able to be combined.

After all data has been aligned temporally, we calculate an offset to bring the wide-scan lidar into the frame of reference of the narrow-scan lidar, effectively removing any inter-laser bias. For each file that contains narrow and wide-scan data, all points are gridded to a 1 m grid and coincident points found. For each lidar, the mean value is found for this selection of points and offset calculated using the following equation:

$$W_{offset} = mean(ATM_{wide}) - mean(ATM_{narrow}) \quad (30)$$

This difference is then applied to all wide-scan points within the entire file:

$$ATM_{wide} = ATM_{wide} + W_{offset} \quad (31)$$

As each file will contain different amounts of wide/narrow-scan overlap, the following rules are used for adjusting each file: 1) If the file contains only narrow-scan data, all offsets simply remain zero. 2) If the offset is greater than +/- 0.05 m, then it is determined that the inter-laser differences are too large and all wide-scan data is removed from this file. 3) If the file contains only wide-scan data, the mean of all valid W_{offset} values for the flight is calculated and then applied to all data within this file.

Each ATM point is tagged as to its origin (wide/narrow), but the combined data is used throughout the entire processing chain as a single product except when identifying ATM points over DMS identified leads. In this case, only narrow-scan ATM data is used, as it has an increased accuracy and rate of return that negates any contribution additional wide-scan data could offer.

7.2 Error fixes

This section describes errors which were discovered in the version 1 data products and which have been subsequently fixed in the version 2 data set.

7.2.1 Scan angle bias

A scan angle bias was discovered in the ATM elevation data and is described in detail in *Yi et al.*, [2015]. An empirical correction to correct this error is now implemented in the version 2 products, and the recorded elevation correction is now in the product file. The scan angle bias is thought to be related to unresolved mounting biases, thus the applied empirical correction is generated based on files which have similar pitch and roll values. The correction is applied as follows:

Each ATM file containing at least 800,000 points are first utilized to generate corrections. A filter is applied to exclude points which are within two standard deviations of the median pitch and roll value for the file. A longwave elevation filter is then applied to each file by subtracting a 50,000 point smoothing filter, resultant elevations are then filtered to remove any values greater or less than 10 m. All remaining points are then binned based on azimuth values using 10 degree bins, each azimuth bin has the mean value and standard deviation calculated for the elevations found within that 10 degree bin. Each 10 degree bin has the mean subtracted from it in order to not add a bias to the data. The corrected mean value is then linearly interpolated from the 10 degree resolution data. The corrected mean value for each data point is then assigned based upon it's azimuth angle, the value for each point is then turned into a correction which is subtracted from the corrected elevations for each point.

If at any time (before or after data filtering) the number of data points from any ATM file falls below the 800,000 threshold that file is processed separately. This is done by first comparing the mean pitch and roll values from each skipped file against all files with enough points to be used in the initial processing. The corrections from the most comparable file are then applied. If a file contains less than 100,000 points, then it is expected that an insufficient number of points are available to generate a correction, thus a value of zero is recorded for the correction in this file. If a skipped file also does not have mean pitch and roll values that are within one degree of the pitch and roll values of another successfully processed file, than that file is also skipped and a correction of zero is used for all points in the file.

7.2.2 Sea surface height interpolation

An error in the sea surface height interpolation processing code was discovered which caused the formation of singular covariance matrices and reverted the interpolation to a purely distance weighted approach. This may have caused discontinuities in the calculated sea-surface height in previous versions. The issue has been fixed and the ordinary kriging approach described above is now properly implemented. Covariance matrices which are identified as potentially ill conditioned are now identified in processing, when ill-conditioned matrices are present the sea surface tie points are averaged to a 5 km spacing which has subsequently fixed the problem. In addition to this, non-physical negative weights which occur in the approach are now fixed using the method of *Deutsch*, [1996].

7.2.3 Ocean and load tide errors

The TPXO6.2 tide model has been updated to a newer version, the TPXO8.0 tide model which is used to estimate the h_{ocean} and h_{load} components. In previous uses of the TPXO6.2 model for the 2009-2012 Arctic campaigns, the sign for the tidal correction was incorrectly applied. This has been fixed in version 2 products.

7.2.4 Product spacing

An error in the processing code was identified which led to irregular spacing of the 40 m averaged data product. The version 2 product has fixed this error with all data now having a correct spacing of 40

m between the output products. The product spacing is now determined primarily from the snow radar locations and are supplemented by ATM and aircraft position files to ensure consistency when snow radar data gaps or inconsistencies are present.

7.2.5 Snow radar averaging

An error in the previous product version was discovered which utilized only a single snow radar measurement within the 40 m averaged data product, rather than the mean of all measurements within the 40 m average segment. This issue has now been fixed.

8 Acknowledgments

We would like to thank the entire Operation IceBridge crew, instrument teams, and mission managers for their extraordinary efforts in gathering the data used in these products. We acknowledge Vincent Onana for his expertise in desiging an automated lead detection scheme which greatly improved the speed and quality with which these data products can be produced. We would also like to thank the entire IceBridge sea ice science team for their efforts in reviewing and providing suggestions to improve the products. Specifically, we would like to thank Ron Lindsay for his suggestions on improving the quality and usability of the data, Sinead Farrell for providing input on the documentation and sea surface height determination, Ron Kwok for his diligence in improving instrument data quality, Michael Studinger and Jackie Richter-Menge for providing excellent leadership and support throughout the product development stage.

9 References

Andersen et al., The DTU10 global Mean sea surface and Bathymetry. Presented EGU-2008, Vienna, Austria, April, 2008.

Andersen O. B, Knudsen P., The DNSC08 mean sea surface and mean dynamic topography. *J. Geophys. Res.*, 114, C11, doi:10.1029/2008JC005179, 2009.

Carrère, L., and F. Lyard (2003), Modeling the barotropic response of the global ocean to atmospheric wind and pressure forcing - comparisons with observations, *Geophys. Res. Lett.*, 30, 1275, doi:10.1029/2002GL016473, 6.

Cavalieri, D., T. Markus, and J. Comiso. 2004, updated daily. AMSR-E/Aqua Daily L3 12.5 km Brightness Temperature, Sea Ice Concentration, & Snow Depth Polar Grids V002, April 2009. Boulder, Colorado USA: National Snow and Ice Data Center. Digital media.

Chelton, D. B., J. C. Ries, B. J. Haines, L. Fu, and P. S. Callahan (2001), Satellite altimetry, in *Satellite Altimetry and Earth Sciences*, Int. Geo-phys. Ser., vol. 19, Elsevier, New York.

Chelton, D. B., Roland A. deSzoeke, Michael G. Schlax, Karim El Naggar, Nicolas Siwertz, 1998: Geographical Variability of the First Baroclinic Rossby Radius of Deformation. *J. Phys. Oceanogr.*, 28, 433–460.

Cressie, N., 1993, *Statistics for spatial data*, Wiley Interscience.

Deutsch, C. V., 1996, Correcting for negative weights in ordinary kriging: *Computers & Geosciences*, v. 22, no. 7, p. 765–773.

Dominguez, Roseanne. 2009, updated current year. IceBridge DMS L1B Geolocated and Orthorectified Images, [Mar. 15 - Apr. 21, 2010-2011]. Boulder, Colorado USA: National Snow and Ice Data Center. Digital media.

Farrell, S.L., N.T. Kurtz, L. Connor, B. Elder, C. Leuschen, T. Markus, D.C. McAdoo, B. Panzer, J. Richter-Menge, J. Sonntag (2012), A First Assessment of IceBridge Snow and Ice Thickness Data over Arctic Sea Ice, *IEEE Trans. Geosc. Rem. Sens.*, 50 (6), doi:10.1109/TGRS.2011.2170843.

Egbert, G.D., and L. Erofeeva, Efficient inverse modeling of barotropic ocean tides, *Journal of Atmospheric and Oceanic Technology*, 19, N2, 2002.

Krabill, W. B. 2009, updated current year. IceBridge ATM L1B Qfit Elevation and Return Strength, [Mar. 23 - Apr. 21, 2009-2010]. Boulder, Colorado USA: National Snow and Ice Data Center. Digital media.

Krabill, W. B. 2009, updated current year. IceBridge CAMBOT L1B Geolocated Images, [Mar. 15 - Apr. 25, 2009-2011]. Boulder, Colorado USA: National Snow and Ice Data Center. Digital media.

- Krabill, W. B. 2011, IceBridge Narrow Swath ATM L1B Qfit Elevation and Return Strength. Version 1. [Mar. 15 - April 15, 2011]. Boulder, Colorado USA: NASA DAAC at NSIDC.
- Kovacs, A., Sea ice: Part II. Estimating the full-scale tensile, flexural, and compressive strength of first-year ice, *CRREL Rep. 96-11*, Cold Reg. Res. and Eng Lab., Hanover, NH, 1996.
- Kurtz, N. T., Farrell, S. L., Studinger, M., Galin, N., Harbeck, J. P., Lindsay, R., Onana, V. D., Panzer, B., and Sonntag, J. G.: Sea ice thickness, freeboard, and snow depth products from Operation IceBridge airborne data, *The Cryosphere*, 7, 1035–1056, doi:10.5194/tc-7-1035-2013, 2013.
- Kurtz, N. T. and S. L. Farrell (2011), Large-scale surveys of snow depth on Arctic sea ice from Operation IceBridge, *Geophys. Res. Lett.*, 38, L20505, doi:10.1029/2011GL049216.
- Kurtz, N. T., T. Markus, S. L. Farrell, D. L. Worthen, and L. N. Boisvert (2011), Observations of recent Arctic sea ice volume loss and its impact on ocean-atmosphere energy exchange and ice production, *J. Geophys. Res.*, 116, C04015, doi:10.1029/2010JC006235.
- Kwok, R. and G. F. Cunningham (2008), ICESat over Arctic sea ice: Estimation of snow depth and ice thickness, *J. Geophys. Res.*, 113, C08010.
- Kwok, R., G. F. Cunningham, S. S. Manizade, and W. B. Krabill (2012), Arctic sea ice freeboard from IceBridge acquisitions in 2009: Estimates and comparisons with ICESat, *J. Geophys. Res.*, 117, C02018, doi:10.1029/2011JC007654.
- Kwok, R., B. Panzer, C. Leuschen, S. Pang, T. Markus, B. Holt, and S. Gogineni (2011), Airborne surveys of snow depth over Arctic sea ice, *J. Geophys. Res.*, 116, C11018, doi:10.1029/2011JC007371.
- Leuschen, Carl. 2009, updated current year. IceBridge Snow Radar L1B Geolocated Radar Echo Strength Profiles, [Mar. 15 - Apr. 21, 2009-2011]. Boulder, Colorado USA: National Snow and Ice Data Center. Digital media.
- Onana, V.D., N.T. Kurtz, S.L. Farrell, L.S. Koenig, M. Studinger, and J.P. Harbeck (in press), A Sea Ice Lead Detection Algorithm For Use With High Resolution Visible Imagery, *IEEE Trans. Geosc. Rem. Sens.*, doi:10.1109/TGRS.2012.2202666.

Raney, R.K. The delay/Doppler radar altimeter, *IEEE Trans. Geosc. Rem. Sens.*, vol.36, no.5, pp.1578-1588, Sep 1998 doi: 10.1109/36.718861.

Schenk, T., B. M. Csatho and D-C. Lee, 1999. Quality control issues of airborne laser ranging data and accuracy study in an urban area. *International Archives of Photogrammetry and Remote Sensing*, 32(3 W14), 101-108.

Shetter, Rick, Eric Buzay, David Van Gilst. 2010, updated current year. IceBridge NSERC L1B Geolocated Meteorologic and Surface Temperature Data, [Mar. 23 - Apr. 21, 2010]. Boulder, Colorado USA: NASA Distributed Active Archive Center at the National Snow and Ice Data Center. Digital media. <http://nsidc.org/data/iamet1b.html>.

Tiuri, M., A. Sihvola, E. Nyfors, and M. Hallikainen (1984), The complex dielectric constant of snow at microwave frequencies, *IEEE J. Oceanic Eng.*, 9(5), 377 – 382.

Wadhams, P., W.B. Tucker III, W.B. Krabill, R.N. Swift, J.C. Comiso, and N.R. Davis (1992), Relationship between sea ice freeboard and draft in the Arctic basin, and implications for ice thickness monitoring, *J. Geophys. Res.*, 97, C12, 20325-20334.

Wahr J. M., Deformation induced by polar motion, *J. Geophys. Res.*, 90(B11): 9363 - 9368, 1985.

Warren, S. G., I. G. Rigor, N. Untersteiner, V. F. Radionov, N. N. Bryazgin, Y. I. Aleksandrov, and R. Colony (1999), Snow depth on Arctic sea ice, *J. Climate*, 12 (6), 1814-1829.

Webster, M. A., I. G. Rigor, S. V. Nghiem, N. T. Kurtz, S. L. Farrell, D. K. Perovich, and M. Sturm (2014), Interdecadal changes in snow depth on Arctic sea ice, *J. Geophys. Res. Oceans*, 119, 5395–5406, doi:10.1002/2014JC009985.

Weller, G., Radiation flux investigation, *AIDJEX Bull.*, 14, 28-30, 1972.

World Meteorological Organization, *Sea ice nomenclature: Terminology, Codes and Illustrated Glossary*, WMO/OMM/BMO 259, TP 145, World Meteorological Organization, Geneva, 1970.

Yi, D., Harbeck, J.P., Manizade, S.S., Kurtz, N.T., Studinger, M., Hofton, M., Arctic Sea Ice Freeboard Retrieval With Waveform Characteristics for NASA's Airborne Topographic Mapper (ATM) and Land,

Vegetation, and Ice Sensor (LVIS), IEEE Trans. Geosc. Rem. Sens., vol.53, no.3, pp.1403-1410, doi: 10.1109/TGRS.2014.2339737, 2015.

10 Appendix: Mission, campaign, and flight specific notes

10.1 Arctic 2009 campaign

Identification of leads was accomplished using CAMBOT data, rather than DMS data which was not available for this campaign. Due to the orientation of the camera and time between images, the CAMBOT data do not cover the entire flight track. At the nominal flight altitude and speed, the images span about 70% of the flight track. For example, at a flight altitude of 450 m each image covers 340 m in the along track direction, while the plane covers ~490 m in the 5 seconds between images, thus about $150/490 = \sim 30\%$ of each flight line missing in the imagery. The return flight on April 21, 2009 was at a high altitude and full coverage of the flight line was obtained.

The ATM elevation data have been shown to contain a small bias for data with a low return energy, the correction factor described in *Kwok et al.*, [2012] has been implemented for this campaign.

The KT19 instrument was not available during this campaign.

10.1.1 March 31, 2009: Fram Strait flight

No snow depths are reported for this day. This was the first flight with the snow radar and the radar transmit power was set to a level twice as high as was used in subsequent flights. Receiver saturation problems were present in the data files which lowers the quality of snow depth retrievals which can be obtained from this flight. The retrieved snow depth values were on average ~50 cm and frequently exceeded the retrieved sea ice freeboard.

10.1.2 April 5, 2009

Due to a malfunction of the CAMBOT sensor, CAMBOT coverage for this day only spanned a limited portion of the flight line. This limited the amount of freeboard data which could be retrieved for this day.

10.1.3 April 21, 2009

Surface temperatures near the end of this flight reached as high as $-4\text{ }^{\circ}\text{C}$ which appeared to impact the snow radar data. These data have been discarded. This flight consisted of outbound and return sections where the same flight line was repeated at two different altitudes. On the higher altitude inbound portion of the flight the snow radar was unable to distinguish the snow-air interface from the noise level due to the lower return energy, no snow depth values are reported for the inbound portion of the flight.

10.1.4 April 25, 2009

Caution is urged when using data near landmasses during this flight, the use of an interpolated sea surface height over large distances may not be applicable in these instances due to local inaccuracies in the geoid and tide models. We have also attempted to remove all data which were over land during this flight.

10.2 Arctic 2010 campaign

Identification of leads was accomplished using DMS imagery for this campaign. The adjusted mean freeboard field (fb_{adj}) is reported for this and subsequent campaigns and represents the derived freeboard from the combined ATM and DMS data sets. Surface temperature data from the KT19 instrument is also reported in this data set, however the KT19 internal temperature was not recorded during this campaign. The surface temperature data were recorded using a 1 Hz averaging rate, thus the surface temperatures reported here are an average over an area equal to the distance the aircraft traveled in one second. The emissivity setting of the KT19 instrument was set to 1 for the surface temperature retrievals during this campaign, a correction described in the previous section has been applied to bring the temperatures to that of a surface with emissivity of 0.97.

A modified low energy correction for the ATM elevation data was needed for this campaign due to the use of different laser components. The new low energy correction, h_{e-corr} (in units of meters) was derived using calibration data provided by the ATM instrument team. Similar to the low energy correction of *Kwok et al.*, [2012], the new correction is an 8th order polynomial fit of the calibration data which is added to the ATM elevation data:

$$h_{e-corr} = 1.356 \times 10^{-26} r_s^8 - 1.51483 \times 10^{-22} r_s^7 + 7.48991 \times 10^{-19} r_s^6 - 2.16621 \times 10^{-15} r_s^5 + 3.97857 \times 10^{-12} r_s^4 - 4.61175 \times 10^{-9} r_s^3 + 3.17998 \times 10^{-6} r_s^2 - 0.00118755 r_s + 0.2$$

where r_s is the ATM relative reflected laser signal strength. This polynomial was chosen to correct for biases to the level of points with a relative received amplitude of 1100, which was the most frequently observed reflected signal strength during the 2010 Arctic campaign. A constant correction of 0.008 meters is added to points with a relative amplitude greater than 2500 to most accurately correspond with the calibration data set.

10.3 Arctic 2011 campaign

A centroid waveform fitting has been used in the surface elevation retrievals for the ATM data in this campaign. This method eliminates the “range walk” associated with the previous leading edge fit procedure, and thus no low energy elevation correction scheme was applied for this and subsequent campaigns. The ATM “narrow-swath” data (Krabill, 2011) were first introduced during this campaign. The narrow-swath instrument allowed for a much larger number of returns over leads and smooth ice surfaces to be used in the freeboard retrieval processes compared to previous campaigns.

10.3.1 March 17, 2011

There was significant data loss due to clouds leading to gaps in the data for part of this flight. Additionally, DMS data were not available for the entire flight for the detection of leads. Where available the DMS data were used, but CAMBOT data were used for the time period spanning approximately 14:00-16:30 UTC time.

10.3.2 March 22, 2011

Cloudy conditions were present during much of this flight which led to only sparse data coverage for this flight (see the mission flight report for more details: <http://nsidc.org/data/ifttrpt.html>). CAMBOT data were used for the detection of leads up to approximately 17:25 UTC time due to the absence of DMS data.

10.3.3 March 23, 2011

A timing error in the snow radar data files led to a 15 second offset between the matching of the time stamp and geolocation data in the original data files. This error was corrected in the final processing of the data products. (Thanks to Tom Newman for discovering the error.)

10.3.4 March 25, 2011

CAMBOT data were used for the detection of leads up to approximately 14:50 UTC time due to the absence of DMS data. The first ~2 hours of the data line were flown in darkness and no visible imagery was available for lead detection and retrieval of freeboard.

10.3.5 March 28, 2011

Due to large errors in the EGM08 data set for the Nares Strait region the freeboard and thickness retrievals are only valid very close to sea surface tie points. We have set the freeboard and thickness retrievals for the first 10 minutes of the flight to invalid values due to this issue.

10.3.6 April 15, 2011

No leads were identified in the DMS and CAMBOT images for the determination of sea surface height, thus no sea ice freeboard and thickness estimates were made.

10.4 Arctic 2012 campaign

The ATM narrow-swath data (Krabill, 2011) were used for all but two flights (listed below) during this campaign. The data were combined with the wide-scan instrument to retrieve surface elevation and freeboard.

The KT19 infrared pyrometer was also operated during this campaign, the response setting was 3 Hz which allowed for higher resolution surface temperature measurements to be made. The KT19 emissivity was set to 0.97 for this campaign.

10.4.1 March 14 (North Basin Transect, Thule-Fairbanks)

A hardware failure by the snow radar data recording system led to a section of missing data during the flight.

10.4.2 March 15 (Beaufort-Chukchi Zig Zag)

An undetermined source of coherent noise was present in the snow radar data throughout the flight. This noise impacts the quality of the retrievals and thus the quality of the snow depth data may be lower for this flight. The additional noise led to the original snow depth retrieval algorithm to incorrectly identify areas with high noise as the location of the snow-air interface. To mitigate this, we have added additional requirements for the selection of the snow-air interface for this flight. Equation 18 has been changed to

$$\overline{P_{s-a}} \geq \hat{P}_{s-a}^{min} + 10 \quad (32)$$

An additional requirement following equation 18 for the identification of the snow-air interface has been added:

$$\overline{\overline{P_{s-a}}} \geq \hat{P}_{s-a}^{min} + 10 \quad (33)$$

where $\overline{\overline{P_{s-a}}}$ is the mean power in range bins 7-14 that follow \hat{P}_{s-a}^{min} . Since the additional noise for this flight occurs as areas of moderately high power levels followed by a return to a low level background noise, these

additional requirements reduce the likelihood that areas of high noise will be selected as the snow-air interface while keeping the core snow depth retrieval algorithm intact.

10.4.3 March 17 (Alaska Coastal Zig Zag A) and March 19 (South Basin Transect, Fairbanks-Thule)

Due to an instrument failure, the narrow scan ATM was not available for these flights. The wide scan ATM was used instead.

10.4.4 March 16 (Alaska Diamond), 17 (Alaska Coastal Zig Zag A), and 22 (Connor Corridor)

Only several leads were found in these flights for the retrieval of freeboard and sea surface height. The correlation length and maximum uncertainty of the sea surface height observations are thus not well known and the freeboard and sea ice thickness uncertainty fields should be treated with caution.

10.4.5 March 26 (Wingham Box), March 28 (CryoSat-2 underflight)

No snow depth retrievals are reported for the high altitude portion of these flights since the noise level is expected to exceed the estimated return power from the snow-air interface.

10.5 Antarctica 2009

This marks the first IceBridge campaign in the Antarctic. Three flights were completed in the Weddell and Bellingshausen and Amundsen Sea regions. The data for this campaign have been processed to include freeboard, but not snow depth on sea ice estimates. The snow radar configuration during this campaign was not optimal, there is a large amount of coherent noise in the data due to the antenna placement and the usable bandwidth is lower than in other IceBridge campaigns. This was improved in future IceBridge deployments, but for this campaign we do not make use of the snow radar data for this reason. Additionally, ice type data was not included for the Antarctic campaign.

Concerning the ATM data, the ATM low energy elevation correction used during this campaign is equivalent to that used during the 2010 Arctic campaign. This was done since the laser configurations were the same for both campaigns.

10.6 Antarctica 2010

The Antarctic 2010 was similar to the Antarctic 2009 campaign in that three flights were completed in the Weddell and Bellingshausen and Amundsen Sea regions, all data have been processed in an equivalent manner to the Antarctic 2009 campaign except where noted.

The data for this campaign have been processed to include freeboard, but not snow depth on sea ice estimates. It is not clear to what degree flooding and layering of the snow pack, which in-situ studies have shown are prevalent in Antarctic sea ice, affects the radar signal from the snow radar. Preliminary investigations using the snow depth algorithm used for Arctic sea ice show lower than expected snow depths when compared to the freeboard from the laser altimetry data. Therefore, snow depth estimates from the snow radar for the Antarctic campaigns require more detailed investigation to ensure data quality and are not provided in the present version of the data products. If further research in this area shows viable retrievals can be made with sufficient quality, then they will be included in a future revision of the data set.

Concerning the ATM data, a low energy correction, h_{e-corr} (in units of meters) was derived using calibration data provided by the ATM instrument team. The correction is an 8th order polynomial fit of the calibration data which is added to the ATM elevation data:

$$h_{e-corr} = 1.356 \times 10^{-26} r_s^8 - 1.51483 \times 10^{-22} r_s^7 + 7.48991 \times 10^{-19} r_s^6 - 2.16621 \times 10^{-15} r_s^5 + 3.97857 \times 10^{-12} r_s^4 - 4.61175 \times 10^{-9} r_s^3 + 3.17998 \times 10^{-6} r_s^2 - 0.00118755 r_s + 0.193$$